FRAMEWORK MATERIALS

Molecular recognition with resolution below 0.2 angstroms through thermoregulatory oscillations in covalent organic frameworks

Yiming Hu[1]†, Bratin Sengupta[2]†, Hai Long[3], Lacey J. Wayment[1], Richard Ciora[2], Yinghua Jin[1]‡, Jingyi Wu[1], Zepeng Lei[1], Kaleb Friedman[2], Hongxuan Chen[1], Miao Yu[2]*, Wei Zhang[1]*

Crystalline materials with uniform molecular-sized pores are desirable for a broad range of applications, such as sensors, catalysis, and separations. However, it is challenging to tune the pore size of a single material continuously and to reversibly distinguish small molecules (below 4 angstroms). We synthesized a series of ionic covalent organic frameworks using a tetraphenoxyborate linkage that maintains meticulous synergy between structural rigidity and local flexibility to achieve continuous and reversible (100 thermal cycles) tunability of "dynamic pores" between 2.9 and 4.0 angstroms, with resolution below 0.2 angstroms. This results from temperature-regulated, gradual amplitude change of high-frequency linker oscillations. These thermoelastic apertures selectively block larger molecules over marginally smaller ones, demonstrating size-based molecular recognition and the potential for separating challenging gas mixtures such as oxygen/nitrogen and nitrogen/methane.

Microporous crystalline materials, such as metal and covalent organic frameworks (MOFs and COFs, respectively) and zeolites, have applications in sensing (*1*, *2*), catalysis (*3*–*6*), and molecular separation (*7*–*9*). Conventionally, reticular chemistry (*10*, *11*) and postsynthesis modifications (*12*, *13*) are used to obtain specific pore sizes that meet the requirements of the target applications. Occasionally, some of these materials exhibit flexibility with stimuli-induced pore shape and size tunability (*14*, *15*), enabling pore adjustment within a single material to accommodate target applications.

Flexibility in such materials typically arises from substantial movement of weak bonds [e.g., coordination bonds in MOFs (*15*, *16*)] in response to external stimuli such as the adsorption of molecules (*17*) and changes in temperature (*18*, *19*) or pressure (*20*). This usually triggers relatively large pore size change (3 to 5 Å), exceeding the subangstrom scale required for the selective recognition of small molecules (*16*, *21*, *22*). Materials that rely on local molecular motion can achieve pore adjustment appropriate for molecular separation, for example, to differentiate isotopes (*18*, *23*, *24*) or small hydrocarbons (*25*). These materials differentiate molecules through a diffusion rate difference, which depends on the differences in mass instead of size (*18*, *24*, *25*). However, it remains a challenge to differentiate small molecules based on their true shape and size using crystalline materials with reversible, continuously adjustable pores because achieving pores that fall exactly between the sizes of two molecules requires ultra-high-precision tunability. This necessitates material design that involves a delicate balance between structural rigidity to maintain long-range order and weak molecular motion to allow for local flexibility.

Among possible potential dynamic covalent linkages to construct such precisely tunable crystalline materials, borate chemistry is particularly promising (*26*–*28*). The reversible B–O bond allows precise synthesis of long-range crystalline or even single-crystalline materials, for example, helical covalent polymers (HCPs) and COFs (*28*–*30*). The tetra-oxygen–bonded borate, in particular, has increased local flexibility due to tetrahedral conformation and secondary ionic interactions. For example, the dihedral angle of the tetraborate linkage gets distorted from 90° to 66° in HCPs (*30*). These tetraoxyborate linkages provide the potential to construct structures having both long-range crystallinity and local flexibility.

We report a facile strategy of combining covalent polymerization with interlayer ion-dipole interaction in a crystalline material to achieve meticulous balance of long-range structural rigidity and local molecular flexibility. We used boron chemistry to synthesize a series of crystalline ionic COFs (ICOFs) (Fig. 1A). These ICOFs exhibit reversible, ultraprecise pore tunability with resolution <0.2 Å.

ICOFs with locally flexible tetraphenoxyborate nodes

To synthesize these ICOFs, we started with the simplest building blocks, hydroquinone (**1**) and sodium borohydride, as shown in Fig. 1A. The 2:1 stoichiometric mixture of hydroquin[illegible] and sodium borohydride was heated at 12[illegible] in acetonitrile without any disturbance to yield ICOF-101-Na with an isolated yield of 81%. The infrared (IR) spectrum of ICOF-101-Na shows the absence of O–H stretching at 3300 cm^{-1} and B–H stretching at 2300 cm^{-1} and the presence of a B–O stretching band at 950 cm^{-1} (Fig. 1B). The overall IR spectrum of the ICOF-101-Na closely resembles that of the sodium tetraphenoxyborate (NaTB), a model compound with tetraphenoxyborate linkage, supporting the formation of $[BO_4]^-$ anions (*31*). The chemical structure of ICOF-101-Na was further confirmed by solid-state ^{11}B and ^{13}C nuclear magnetic resonance (NMR) spectroscopy (Fig. 1C and figs. S1 and S2). In the solid-state ^{11}B NMR spectrum, a characteristic signal corresponding to tetra-substituted boron was observed at 2.06 ppm, which is consistent with the boron resonance signal observed for NaTB, suggesting the formation of a tetraphenoxyborate linkage. The single resonance in the ^{11}B NMR spectrum of ICOF-101-Na indicated negligible defect sites within the frameworks. Additionally, two sharp signals observed at 120 and 150 ppm in the ^{13}C NMR spectrum also support the highly symmetrical chemical environment in ICOF-101-Na (fig. S1).

The powder x-ray diffraction (PXRD) pattern at room temperature confirmed the crystallinity of ICOF-101-Na with no observable diffraction peaks from the starting materials, hydroquinone and sodium borohydride (Fig. 1D). For a tetrahedral-shaped, node-based extended structure, *dia* topology is commonly observed or adopted irrespective of connection types and linkers (*32*, *33*). Thus, we first modeled the framework using tetraphenoxyborate linkage as tetrahedral nodes in *dia* topology and assumed free positioning of the sodium counterion. However, none of these generated models, including various interpenetration folds, matched the experimental PXRD pattern, suggesting that the sodium ion may interfere with the solid-state structure of the framework (fig. S3 and table S1).

Inspired by the crystal structure of the NaTB, where the sodium ion is weakly bound with tetraphenoxyborate linkage (*31*), we built a layered two-dimensional (2D) structure for ICOF-101-Na in a space group of P4/N, where the tetrahedral nodes propagate in the same plane. The unit cell parameters ($a = b = 10.6850$ Å, $c = 5.7690$ Å, $\alpha = \beta = \gamma = 90°$) were obtained and further refined with Pawlay fitting, which showed a good agreement factor with experimental PXRD diffraction (Rp = 1.27% and Rwp = 2.07%; Fig. 1D and table S2). In our modeled structure, four phenyl groups were joined together by strong covalent tetraphenoxyborate linkages and further extended in the planar direction (Fig. 1E). As shown in Fig. 1D, the (110) facet on PXRD validated the

[1]Department of Chemistry, University of Colorado Boulder, Boulder, CO 80309, USA. [2]Department of Chemical and Biological Engineering and RENEW Institute, University at Buffalo, Buffalo, NY 14260, USA. [3]Computational Science Center, National Renewable Energy Laboratory, Golden, CO 80401, USA.
*Corresponding author. Email: myu9@buffalo.edu (M.Y.); wei.zhang@colorado.edu (W.Z.)
†These authors contributed equally to this work.
‡Present address: RockyTech Ltd., Boulder, CO 80309, USA.

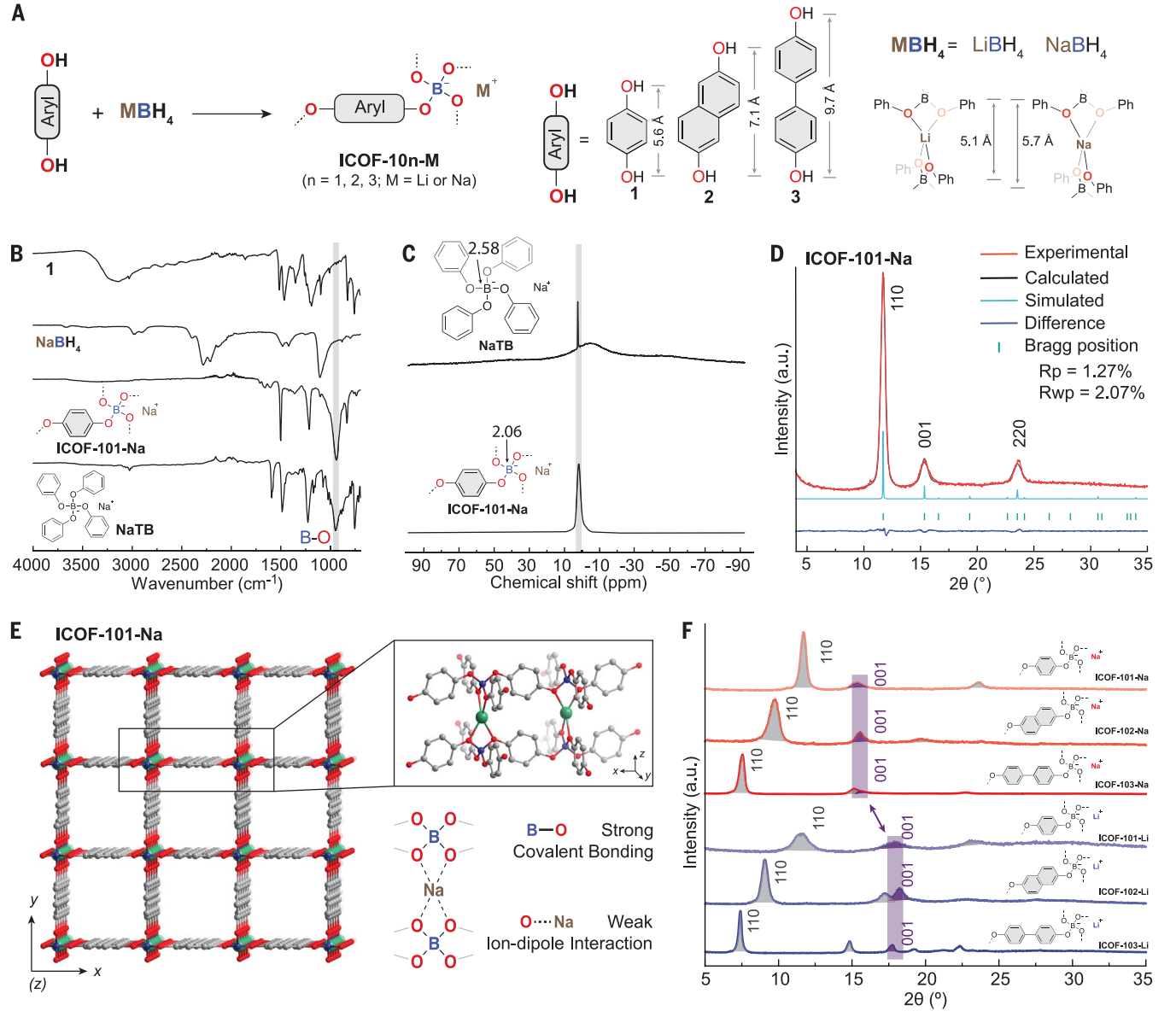

Fig. 1. Rational design and synthesis of 2D ICOFs. (**A**) General synthesis strategy for ICOF-10n-M through the condensation reaction between a variety of diol linkers and boron sources. The *n* can be 1, 2, or 3 depending on the linker as marked on the right side, Aryl is phenyl, and M is the metal (Na or Li). As an example, the ICOF-101-Na was characterized by Fourier transform infrared (FTIR), ^{11}B NMR, and PXRD spectroscopy. (**B**) FTIR spectra of **1**, sodium borohydride, ICOF-101-Na, and NaTB. (**C** and **D**) ^{11}B NMR of NaTB (C) and ICOF-101-Na and PXRD patterning of ICOF-101-Na and its refinement (D). The experimental pattern is shown in red, the Pawley refined pattern in black, the simulated pattern in light blue, the Bragg position in green, and the difference between the observed and refined patterns in navy blue. Rp, residual error; Rwp, weighted residual error. (**E**) Crystal structure of ICOF-101-Na. The layers are cross-linked with a strong covalent tetraphenoxyborate bond on the *x*–*y* plane and extend in the vertical direction through a weak ion-dipole interaction. C is shown in gray, B in blue, Na in green, and O in red. H is omitted for clarity. (**F**) Isoreticular series (ICOF-10n-M) demonstrating the generalizability of this approach and the tunability of aperture size. PXRD patterns show that with increasing length of diol linkers, a shift of (110) peak to the lower 2θ was observed, whereas with a decreasing of interlayer distance, the (001) peak shifted to the higher 2θ area.

square repeating unit cell that is connected by four hydroquinones through a strong tetraphenoxyborate linkage. We verified the presence of the weak ion-dipole interaction between the oxygen atoms and metal ions along the *z* axis by observing the (001) peak at 15.10°. The sodium counterions are bridged by four oxygen atoms of borate anions from the adjacent layers, forming an alternating organic cationic and metal ion layer in a 2D layered structure. To validate the layered model, we calculated the interlayer distance using the Na–O distance from the single-crystal structure of NaTB, and found that it matched very well with the $d_{(100)}$ spacing (5.9 Å) observed in the PXRD pattern of ICOF-101-Na (see the supplementary text, section S1). We also performed variable-temperature PXRD experiments over a range of 25 to 200°C and detected no apparent peak shifts (fig. S4), demonstrating the thermal stability of the crystalline structure.

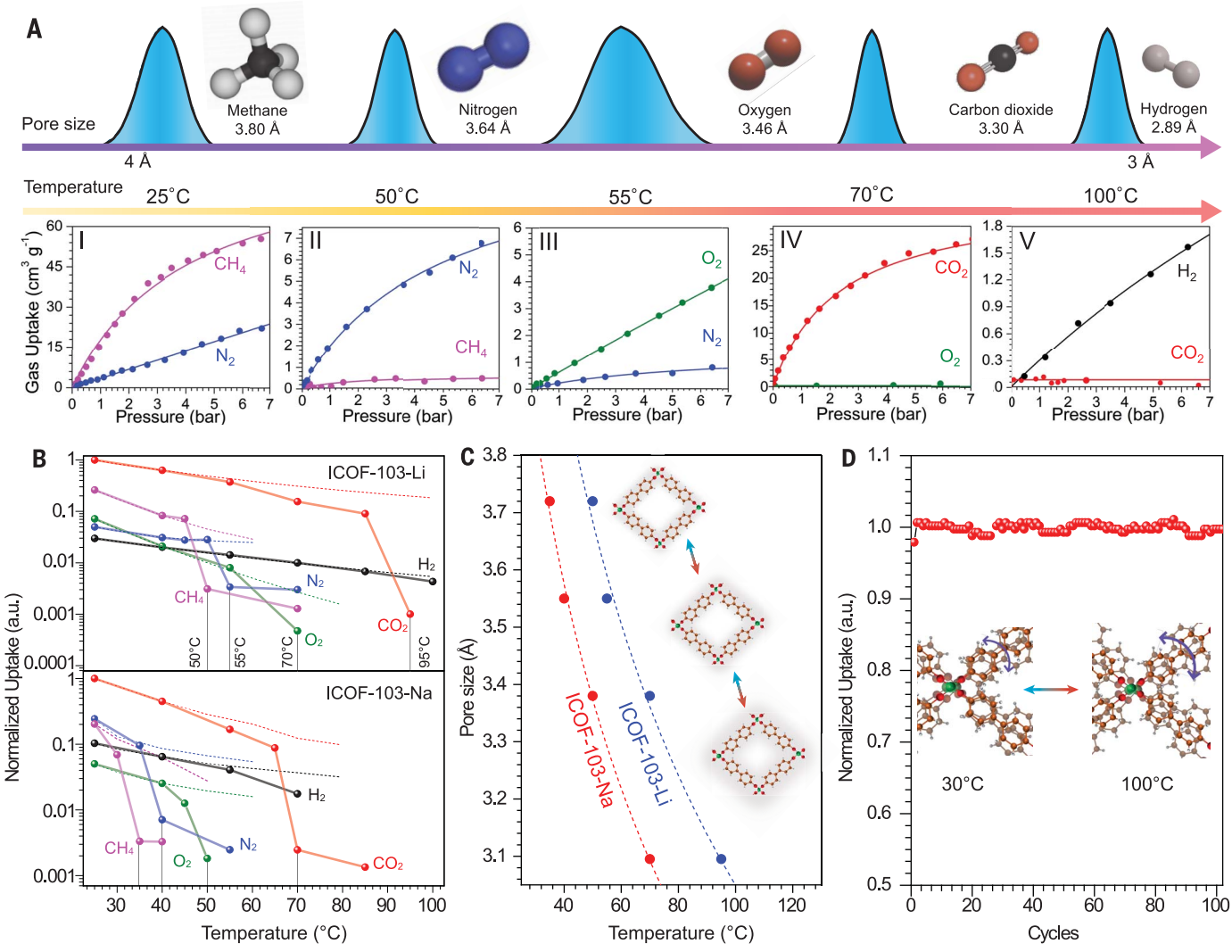

Fig. 2. Subangstrom-scale precise thermoregulatory molecular sieving of ICOFs. (**A**) Regulation of effective pore size of ICOF through temperature. Top: expected pore size distribution (based on isotherms below) changes within the narrow range between 3 and 4 Å as shown relative to the gas molecules. Bottom: isotherms for different gases at different temperatures. From left to right: I, CH_4 and N_2 at 25°C; II, CH_4 and N_2 at 50°C; III, N_2 and O_2 at 55°C; IV, O_2 and CO_2 at 70°C; and V, CO_2 and H_2 at 100°C for ICOF-103-Li. (**B**) Normalized gas uptake at 1 bar (points and solid lines) and different temperatures for ICOF-103-Li (top) and ICOF-103-Na (bottom). The gas uptake is normalized by CO_2 uptake at 25°C and 1 bar. Dashed lines indicate the estimated uptake for the gases normalized by CO_2 uptake at 25°C and 1 bar. (**C**) Continuous changing of pore size of ICOF with temperature. The effective pore size at a given temperature can be predicted by following the dashed line. Gray regions show the spaces occupied by the oscillation of organic linker, which occupies more space at higher temperature, yielding a smaller effective pore size (top to bottom). (**D**) Reversible dynamic gating behavior for ICOF-103-Na. CO_2 uptake at 25°C and 1 bar (normalized by its capacity at cycle 1) over 100 cycles of heating and cooling between 25° and 100°C. Purple arrows illustrate the oscillatory movement of the organic linker in each cycle showing the change from a low-amplitude oscillatory state at low temperature to a higher-amplitude oscillatory state at higher temperature. The volumetric gas uptake values are at standard temperature and pressure.

Tetraphenoxyborate chemistry: General strategy for constructing ICOFs

After demonstrating the feasibility of tetraphenoxyborate chemistry to construct a crystalline ICOF, we further advanced the versatility of this approach through isoreticular expansion of ICOF-101-Na in both the horizontal direction by introducing the expanded linkers of 2,6-dihydroxynaphthalene (**2**) and 4,4′-biphenol (**3**) and in the vertical direction by intercalating the lithium ion, as shown in Fig. 1A. The corresponding ICOFs (five additional ICOFs from ICOF-102-Na to ICOF-103-Li) were synthesized and characterized in the same fashion as ICOF-101-Na (figs. S5 to 23 and tables S2 to S9); they followed the expected pattern of isoreticulation and exhibited similar spectroscopic and PXRD patterns (Fig. 1F). In particular, a gradual shift of the lowest-angle diffraction peak corresponding to the (110) facet was observed from the ICOF-101 to ICOF-103 series, which agrees with the increased linker lengths of phenyl, naphthyl, and biphenyl and thus the increased size of the pore channels. All Na-series ICOFs exhibited a 2θ peak at around 15.0° on the (001) facet, suggesting the interlayer distance generated by the coordination of sodium ions between two anion layers. Conversely, all Li-series ICOFs exhibited a (001) facet peak at around 17.5°, which was shifted by 2.5° from the Na series because of the shorter Li–O distance and the resulting shorter interlayer distance.

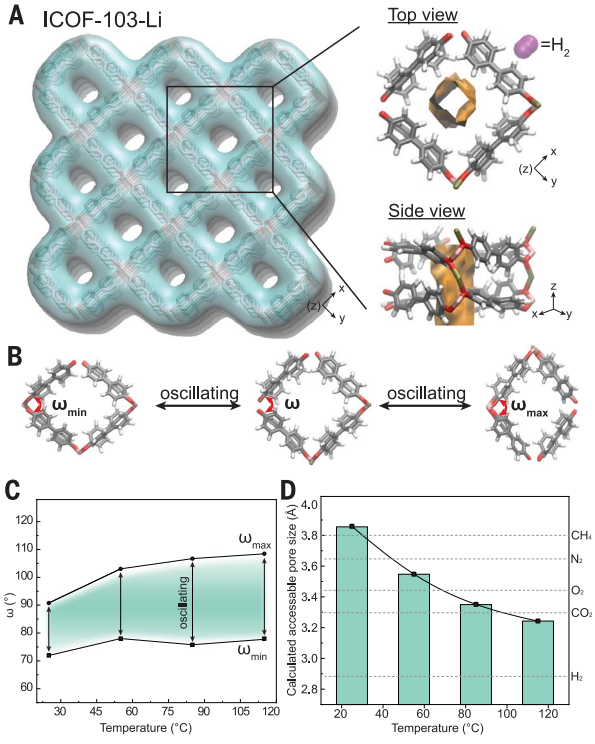

Fig. 3. Computational modeling of temperature-dependent structural changes in ICOFs. (**A**) Left: structure of ICOF-103-Li calculated from AIMD simulations. The channels formed due to stacking of the layered structure. Right: top view and side view of the substructure showing the isosurface at 25°C (in orange), which indicates the actual pore for gas adsorption. The hydrogen gas molecule (top right corner) provides an estimate of the diameter of this isosurface. (**B**) Three snapshots of substructures showing the oscillation behavior. ω, the B–B–B angle in the *x*–*y* plane, changes from ω_{min} and ω_{max} during the oscillation. (**C**) The amplitude of the linker oscillation increases with temperature, manifesting in a larger change from ω_{min} and ω_{max} at higher temperatures. This increase in the amplitude manifests in a pore size change. (**D**) The aperture size change of ICOF-103-Li is in the range of size differences of gas molecules.

We also demonstrated facile synthesis of ICOF on a 10-g scale (fig. S23 F).

Temperature-regulated pore size tuning in ICOFs

Crystalline microporous materials are promising for gas storage and separation (*8*, *13*, *19*). Given the porous nature of the ICOF structures, we investigated the gas adsorption behavior under thermodynamic equilibrium conditions for ICOF-103-Na and ICOF-103-Li, which have the highest crystallinity among all of the synthesized ICOFs. A home-built, well-calibrated, volumetric gas adsorption system (fig. S24) was used to measure adsorption isotherms up to 7 bar (figs. S25 to S34) for different gases (H_2, CO_2, O_2, N_2, and CH_4; properties are described in table S10) having kinetic diameter between 2.89 and 3.80 Å, with only small (<0.2 Å) differences in their sizes and negligible variation in their geometry (except for CH_4) (*34*, *35*).

At 25°C, ICOF-103-Li adsorbs N_2 and CH_4 (Fig. 2, A, I), indicating that both large molecules can easily access the pores. Uptake of the larger CH_4 molecule is significantly higher than that of N_2 (ideal selectivity of CH_4/N_2 = 4.96 at 1 bar) resulting from its octupole moment and thus stronger affinity (*36*). However, when we measured isotherms at 50°C (Fig. 2A, II), CH_4 uptake decreased ~85 times, whereas N_2 uptake decreased only 1.8 times, leading to reversed, size-dependent selectivity of N_2 over CH_4 (ideal selectivity of N_2/CH_4: ~10 at 1 bar). Thus, CH_4 faces difficulty in accessing pores of ICOF-103-Li, whereas N_2, which is only 0.16 Å smaller, can still easily enter. We suspect that this significant decrease of gas uptake of larger molecules may be attributed to a change in the effective pore size of ICOF-103-Li resulting from temperature change. To further investigate this potential pore shrinkage due to temperature, we measured gas uptake at 55°C and found N_2 molecules being effectively blocked by ICOF pores at this temperature. However, O_2 molecules (~0.18 Å smaller) could still access the pores and be adsorbed (Fig. 2A, III), probably suggesting further pore shrinkage. At 70°C, O_2 exhibited negligible uptake, whereas CO_2 (~0.16 Å smaller) was readily adsorbed (Fig. 2A, IV). At 100°C, the effective pore size seemed to have become so small that even CO_2 was blocked, allowing only the smallest molecule, H_2 (2.89 Å), to access the pores (Fig. 2A, V). We thus hypothesize that the pores in ICOF-103-Li continuously shrink due to temperature change from 25 to 100°C, and thus a desired pore size might be obtained at a specific temperature, as shown in Fig. 2A (top).

This decrease in gas uptake with temperature might also be due to the exothermic nature of adsorption, which reduces gas uptake at higher temperatures (*37*–*39*). We calculated the expected uptake for the gases at different temperatures on the basis of their measured adsorption isotherms at the lowest temperatures (see the supplementary text, section S2). This allowed us to estimate the uptake values at different temperatures, assuming that the porous materials would maintain the same structure and surface properties over the temperature range. Figure 2B (top) shows the measured uptake of the five gas molecules at 1 bar, normalized by CO_2 uptake at 1 bar and room temperature, for a temperature range of 25 to 100°C for ICOF-103-Li. A large deviation, one or two orders in magnitude, between the measured uptakes and the calculated uptakes at a specific temperature was observed for all molecules except H_2. The sizeable capacity drop occurred at lower temperatures for larger molecules: for CH_4 at 50°C, for N_2 at 55°C, for O_2 at 70°C, and for CO_2 at 95°C. Apparently, temperature effect on gas uptake cannot exclusively explain this large deviation, and temperature-dependent pore shrinkage might be the dominant reason, as hypothesized. Similar behavior was also observed at higher pressures for ICOF-103-Li (fig. S35). The uptake of molecules with different sizes can be used to define the pore size of porous materials, and the kinetic diameter of these gases suggests that the pores of ICOF-103-Li can be precisely tuned between 2.9 and 3.8 Å by regulating temperature between 50° and 95°C. However, we observed no structural changes at different temperatures from 30° to 200°C in PXRD (fig. S4), suggesting that transient local molecular motions could be responsible for the pore size change (see the discussion on simulation below) (*18*).

Molecular simulation: ICOF structural response to temperature

Aperture change in ICOF-103-Li upon temperature change was investigated by ab initio molecular dynamics (AIMD) simulations. ICOF-103-Li was modeled based on the crystal structure obtained from its PXRD pattern (Fig. 3A). As expected, ICOF-103-Li has a layered structure in the *x*–*y* plane with pores in the *z* direction (Fig. 3A left, and fig. S36). Each layer is composed of quadrilateral substructures in the *x*–*y* plane (Fig. 3A, right) and channels (or pores) along the *z*-axis. The isosurface channel in the middle of these substructures indicates the volume available for gas adsorption, the diameter of which at 25°C is similar to that of small gas molecules (Fig. 3A, right). Our simulation indicates negligible variation in bond lengths within the simulation timescale (table S11). However, transient oscillatory motion of the quadrilateral substructure was observed (Fig. 3B and movie S1). This oscillation was monitored by ω, the angle between three boron atoms in the *x*–*y* plane (B–B–B angle), which was computed from AIMD simulation trajectories (table S12). Because of this oscillation, the angle swung around an initial position, and we defined maximum and minimal angle as ω_{max} and ω_{min}, respectively (Fig. 3B). As

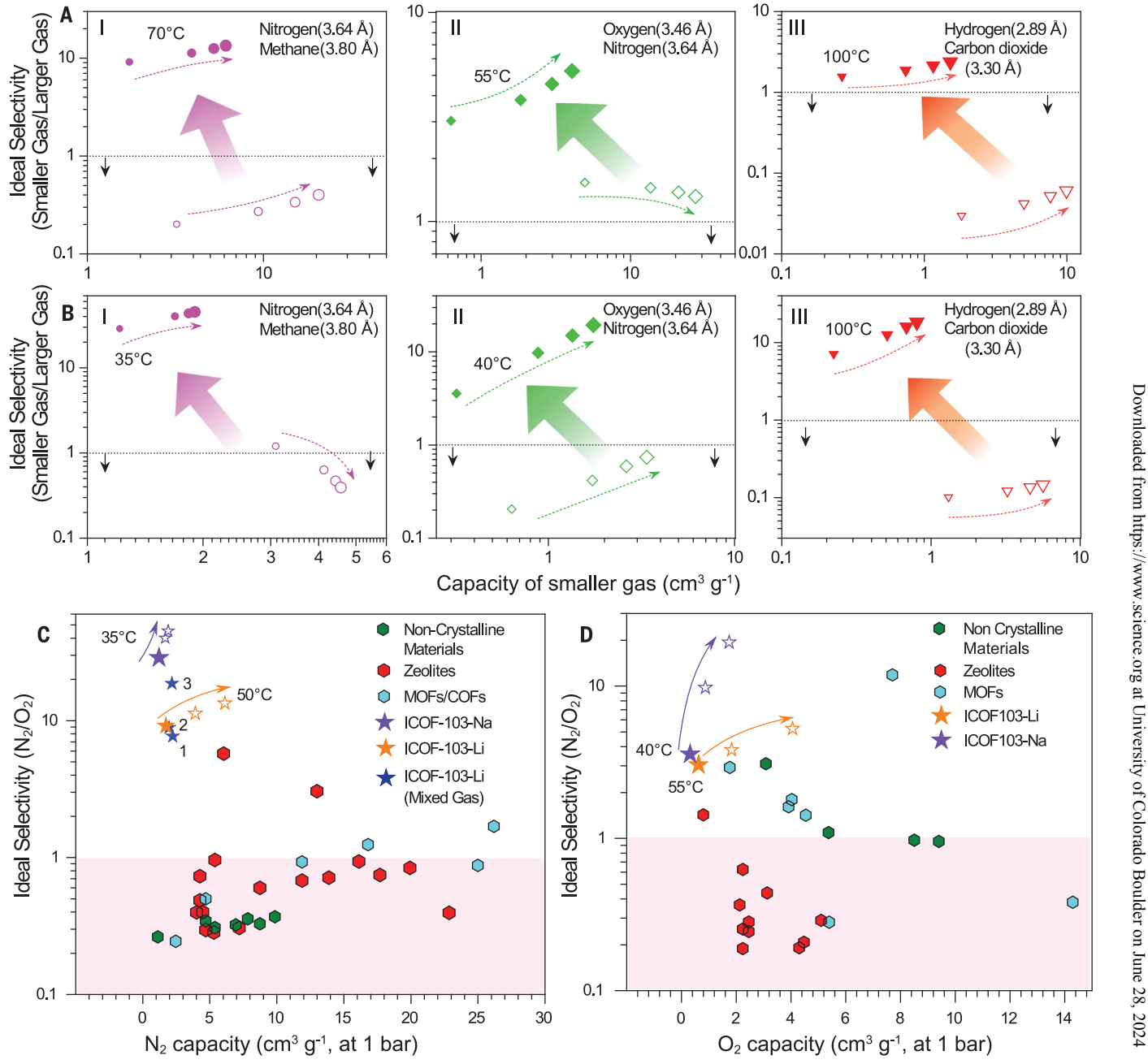

Fig. 4. Adsorptive behavior changes of ICOFs upon temperature change and comparison of ICOFs with reported adsorbents. (**A** and **B**) Ideal selectivity of industrially important gas pairs versus the adsorption capacity of smaller molecules for ICOF-103-Li (A) and ICOF-103-Na (B). Open symbols represent results at 25°C; closed symbols represent results at transition temperatures as labeled. Large solid arrows indicate the adsorptive behavior change from affinity based to size based. Thin dashed arrows (and also the size of the symbols) indicate pressure increase (1, 3, 5, and 7 bar). (**C** and **D**) Adsorptive performance comparison of ICOF and reported adsorbents for N_2/CH_4 (C) and O_2/N_2 (D) based on pure component adsorption isotherms. Solid symbols are data at 1 bar, and open symbols are data at higher pressures (3 and 7 bar). Arrows indicate pressure increase. The blue stars in (C) indicate N_2/CH_4 mixture gas adsorption performance at 50°C. N_2 composition and total pressure are 30 mol % and 4.2 bar (1), 40 mol % and 4.3 bar (2), and 50 mol % and 2.9 bar (3), respectively. Areas shaded in magenta represent sorbents that are selective for CH_4 over N_2 or N_2 over O_2 (affinity-based adsorption). Details of the data points from the literature are provided in tables S16 and S17. The volumetric gas uptake values are at standard temperature and pressure.

temperature increases, the amplitude of the oscillation increases continuously, which causes larger differences between ω_{max} and ω_{min} at higher temperatures (Fig. 3C). This manifests in continuous shrinking of the ICOF pores with temperature, consistent with our gas adsorption results. Temperature change also marginally distorts the substructure. Our theoretical calculation (see the supplementary text, section S3) shows that pore size tunability is within the range of the miniscule size differences of gas molecules (Fig. 3D). The increase of vibrational amplitude with temperature reduces the isosurface volume (fig. S37), indicating pore size reduction. For dynamic pores whose sizes

are determined by oscillation of linkers at the pore mouth, the high oscillation frequency might be essential for preventing approaching gas molecules from entering. Oscillation frequency in ICOFs is calculated to be ~10^{13} s^{-1}, similar to the reported values of some zeolitic imidazolate frameworks (*40*, *41*). At such high frequencies, the time period when the dynamic pores are open to a molecule during an oscillation might be inadequate for it to enter the pores (see the supplementary text, section S4; fig. S38; and table S13). Thus, during oscillation, the smallest aperture size (regulated by amplitude change through temperature) determines the effective pore size. This realizes ultra-high-precision tunability through temperature adjustment, allowing size-dependent molecular recognition with resolution <0.2 Å.

Temperature-engineered ICOFs precisely recognize small molecules

This local molecular movement manifests from the synergistic effect of strong covalent bonds and weaker ion-dipole interactions, providing long-range order as well as local flexibility. We reasoned that such local flexibility to the tetraphenoxyborate linkages permitted relatively free movement of linkers (fig. S39), in strong contrast to more common cases of borate chemistry, in which catechol derivatives are reacted with boric acid (*28*, *42*). Our design permits local flexibility, allowing precise, continuous adjustment of the amplitude of high-frequency oscillation of linkers through temperature adjustment. This enables a reversible, dynamic pore size change in ICOFs, realizing size-dependent molecular recognition with resolution <0.2 Å. Thus, a change in temperature adjusts ICOF pores, leading to the disruption of typical gas uptake behavior. For example, by simply changing the temperature from 25° to 50°C, the ICOF-103-Li pores allow entry of N_2, whereas slightly larger CH_4 molecules are effectively blocked. We refer to this temperature-dependent, size-based molecular recognition as "thermoregulatory molecular sieving" (TRMS). Our simulation indicates that TRMS enables continuous pore adjustment in ICOFs, rather than a few limited discrete states with different pore sizes. Thus, pore adjustment within the subangstrom range manifested by TRMS should allow high selectivity between gas molecules with tiny size differences. In ICOF-103-Na, similar pore adjustment through TRMS was observed at 1 bar (Fig. 2B, bottom), and also at higher pressures (fig. S40; for 3 and 5 bar) between 35 to 70°C. The temperature range for TRMS for ICOF-103-Li and its Na counterpart differs, possibly because of the slightly distorted framework of ICOF-103-Na (fig. S41). This results in "pore shrinking" at lower temperatures compared with ICOF-103-Li. Nevertheless, TRMS continuously adjusts ICOF pores to effectively recognize gas molecules on the basis of their size difference (Fig. 2C). The pore size change does not linearly decrease with temperature. Initially it decreases faster, followed by a much slower change at higher temperatures. This trend is similar to the change of pore size calculated from our AIMD simulation (Fig. 3D and fig. S42). We expect to attain any desired pore size between the sizes of H_2 and CH_4 molecules through careful temperature control (Fig. 2C, schematic).

For materials with such dynamic motion, it remains a concern that they may undergo irreversible structural changes during repeated back-and-forth motion (*43*). To investigate this, we remeasured the CO_2 adsorption isotherm at 25°C after 30 heating-cooling cycles (between 25° and 100°C; figs. S43 and S44) and found no obvious change in the adsorption behavior (tables S14 and 15) for ICOFs. We further subjected ICOF-103-Na to cyclic temperature swings between 30° and 100°C for >100 cycles and gravimetrically measured the change in CO_2 uptake (Fig. 2D). We observed consistent CO_2 uptake (<1% variation) for ICOF-103-Na for 100 cycles, and each cycle involved change from the lower-amplitude to the highest-amplitude oscillation state at two extreme temperatures (Fig. 2D and fig. S45). PXRD patterns for ICOFs before and after 30 heating-cooling cycles also showed no differences (fig. S46), suggesting no obvious structural change. We speculate that the relatively weak ion-dipole interaction allows flexibility, and the strong covalent bond guarantees structural integrity, realizing complete reversibility even after 100 cycles.

Microporous crystalline materials having such precisely tunable, robust, and reversible pores are ideal for adsorptive separation of molecules with almost indistinguishable size and shape differences, such as O_2/N_2 and N_2/CH_4 (*19*, *24*). Figure 4 shows the transition of the adsorption behavior of ICOF-103-Li and ICOF-103-Na for industrially relevant gas pairs and their adsorptive performance comparison for two very challenging gas pairs, O_2/N_2 and N_2/CH_4, with reported microporous materials. We observed affinity-driven selectivity at 25°C. For example, CH_4 uptake is higher than that of N_2, resulting in a N_2/CH_4 selectivity of <1 at all pressures. This is similar to what has been observed in most reported materials (table S16). However, at "sieving temperature" (i.e., the temperature required for transition from affinity to size-based selectivity, which is 70°C for ICOF-103-Li and 35°C for ICOF-103-Na), TRMS enables size-based sieving, leading to N_2/CH_4 selectivity as high as 45 for ICOF-103-Na (and 13.5 for ICOF-103-Li) at 7 bar pressure (Fig. 4A, I and B, I). TRMS is accompanied by some capacity loss. However, achieving this size-based, "reverse selectivity" is extremely challenging and has significant energy savings benefits (*44*), as in the case of N_2 removal from natural gas. ICOFs at sieving temperature show an increase in both selectivity and capacity for the smaller gases with pressure increase. The transition from affinity-based selectivity to size-based selectivity is also evident for other gas pairs (O_2/N_2 and H_2/CO_2) for ICOF-103-Li/Na, where TRMS yields size-based selectivity at the sieving temperatures labeled in Fig. 4, A and B. Thus, by only adjusting the temperature, ICOFs, through their TRMS mechanism, exhibit the potential for separating industrially important gas mixtures (Fig. 4, A and B), including challenging pairs such as O_2/N_2 and N_2/CH_4 (Fig. 4, C and D; figs. S46 to S51; and tables S16 and S17).

The size-dependent selectivity at 50°C was confirmed for N_2/CH_4 gas mixtures as well (table S18), and it is similar to the selectivity calculated using ideal adsorbed solution theory (fig. S52). These results surpass the performance of most current state-of-the-art materials reported in the literature. At 1 bar, both ICOF-103-Na and ICOF-103-Li exhibit higher N_2/CH_4 selectivity than most reported sorbents, with ICOF-103-Na having a selectivity of 28.8 (Fig. 4C). Because higher pressure favors both capacity and selectivity for ICOFs, we observed higher selectivity at 7 bar. In general, ICOF-103-Li provides higher capacity than ICOF-103-Na, albeit achieving lower selectivity. ICOFs through TRMS achieved a N_2/CH_4 selectivity of 45 at 7 bars (Fig. 4C, ICOF-103-Na). Even for O_2/N_2, a selectivity of ~20 was obtained at 7 bars (Fig. 4D, ICOF-103-Na).

Conclusion

We report reversible, ultra-high-precision pore tunability in ICOFs synthesized by easy-access diol building blocks through simple dynamic borate chemistry. Because of the meticulous synergy of strong covalent bonds and weaker ion-dipole interactions in ICOFs, a resolution of <0.2 Å for micropore adjustment over a pore size range of 2.9 to 4.0 Å was obtained upon a temperature change from 25° to 95°C. This precise, temperature-dependent pore shrinkage was controlled by the fast local linker oscillation, the amplitude of which changes with temperature to adjust the pores in ICOFs. Moreover, ICOFs showed excellent structural robustness (up to at least 100 thermal cycles) while maintaining precise, reversible pore tunability. High selectivity for the difficult-to-separate, industrially important gas pairs O_2/N_2 and N_2/CH_4 was observed. Such precision in continuous, reversible pore tunability within a subangstrom scale through TRMS might allow new and more effective uses of microporous crystalline materials in different fields.

REFERENCES AND NOTES

1. E. A. Dolgopolova, A. M. Rice, C. R. Martin, N. B. Shustova, *Chem. Soc. Rev.* **47**, 4710–4728 (2018).
2. X. Liu *et al.*, *Chem. Soc. Rev.* **48**, 5266–5302 (2019).

3. S. Lin *et al*., *Science* **349**, 1208–1213 (2015).
4. Z. Jiang *et al*., *Nature* **586**, 549–554 (2020).
5. M. Zhao *et al*., *Nature* **539**, 76–80 (2016).
6. R. V. Jagadeesh *et al*., *Science* **358**, 326–332 (2017).
7. Z. R. Herm *et al*., *Science* **340**, 960–964 (2013).
8. Y. Belmabkhout *et al*., *Nat. Energy* **3**, 1059–1066 (2018).
9. Q.-F. Lin *et al*., *Science* **374**, 1605–1608 (2021).
10. H. Furukawa, K. E. Cordova, M. O'Keeffe, O. M. Yaghi, *Science* **341**, 1230444 (2013).
11. O. M. Yaghi, M. J. Kalmutzki, C. S. Diercks, *Introduction to Reticular Chemistry: Metal-Organic Frameworks and Covalent Organic Frameworks* (Wiley, 2019).
12. C. Xu, W. Wei, Y. He, *Mater. Lett.* **324**, 132680 (2022).
13. S. Aguado, G. Bergeret, C. Daniel, D. Farrusseng, *J. Am. Chem. Soc.* **134**, 14635–14637 (2012).
14. S. Kitagawa, K. Uemura, *Chem. Soc. Rev.* **34**, 109–119 (2005).
15. J. Dong, V. Wee, D. Zhao, *Nat. Mater.* **21**, 1334–1340 (2022).
16. C. Serre *et al*., *Science* **315**, 1828–1831 (2007).
17. H. Xiong *et al*., *Science* **376**, 491–496 (2022).
18. L. Zhang *et al*., *J. Am. Chem. Soc.* **141**, 19850–19858 (2019).
19. S. M. Kuznicki *et al*., *Nature* **412**, 720–724 (2001).
20. M.-A. Springuel-Huet *et al*., *J. Am. Chem. Soc.* **132**, 11599–11607 (2010).
21. C. Serre *et al*., $^{III}(OH)$-$\{O_2C–C_6H_4–CO_2\}$-$\{HO_2C–C_6H_4–CO_2H\}_x·H_2O_y$. *J. Am. Chem. Soc.* **124**, 13519–13526 (2002).
22. K. Barthelet, J. Marrot, D. Riou, G. Férey, *Angew. Chem. Int. Ed.* **41**, 281–284 (2002).
23. H. Oh *et al*., *Angew. Chem. Int. Ed.* **52**, 13219–13222 (2013).
24. Y. Su *et al*., *Nature* **611**, 289–294 (2022).
25. C. Gu *et al*., *Science* **363**, 387–391 (2019).
26. K. Geng *et al*., *Chem. Rev.* **120**, 8814–8933 (2020).
27. S.-Y. Ding, W. Wang, *Chem. Soc. Rev.* **42**, 548–568 (2013).
28. C. S. Diercks, O. M. Yaghi, *Science* **355**, eaal1585 (2017).
29. A. M. Evans *et al*., *Science* **361**, 52–57 (2018).
30. Y. Hu *et al*., *Nat. Chem.* **13**, 660–665 (2021).
31. I. M. Malkowsky, R. Fröhlich, U. Griesbach, H. Pütter, S. R. Waldvogel, *Eur. J. Inorg. Chem.* **2006**, 1690–1697 (2006).
32. H. M. El-Kaderi *et al*., *Science* **316**, 268–272 (2007).
33. T. Ma *et al*., *Science* **361**, 48–52 (2018).
34. Q. Dong, Z. Song, F. Zhou, H. Li, M. Yu, *Microporous Mesoporous Mater.* **281**, 9–14 (2019).
35. Z. Song *et al*., *ACS Appl. Mater. Interfaces* **10**, 769–775 (2018).
36. F. A. A. Kareem, A. M. Shariff, S. Ullah, N. Mellon, L. K. Keong, *Microporous Mesoporous Mater.* **267**, 221–234 (2018).
37. S. Nandi *et al*., *Sci. Adv.* **1**, e1500421 (2015).
38. M. T. Kapelewski *et al*., *Chem. Mater.* **30**, 8179–8189 (2018).
39. J. A. Mason, M. Veenstra, J. R. Long, *Chem. Sci.* **5**, 32–51 (2014).
40. W. Zhang *et al*., *J. Phys. Chem. C* **122**, 27442–27450 (2018).
41. M. R. Ryder *et al*., *Phys. Rev. Lett.* **113**, 215502 (2014).
42. X. Wang *et al*., *J. Am. Chem. Soc.* **143**, 15011–15016 (2021).
43. H. Deng, M. A. Olson, J. F. Stoddart, O. M. Yaghi, *Nat. Chem.* **2**, 439–443 (2010).
44. S. Li *et al*., *J. Membr. Sci.* **487**, 141–151 (2015).

ACKNOWLEDGMENTS

Funding: B.S. and M.Y. acknowledge University at Buffalo startup funds for financial support. Y.H. and W.Z. were supported by the National Science Foundation (grant 2108197). K.F. and R.C. were supported by the Department of Energy (DOE grant DE-FE0031730). The AIMD simulation was performed using computational resources sponsored by the DOE Office of Energy Efficiency and Renewable Energy and located at the National Renewable Energy Laboratory. **Author contributions:** Y.H., B.S., W.Z., and M.Y. conceived the project. Y.H., L.J.W., J.W., and H.C. performed experiments for material synthesis and characterizations. B.S. performed gas uptake experiments and thermal gravimetric analysis tests with help from K.F. and R.C. H.L. performed the AIMD simulations. Y.H. and Z.L. performed structural modeling. R.C. and K.F. performed gas mixture adsorption experiments. B.S. and R.C. calculated ideal adsorbed solution theory selectivity. B.S., Y.H., H.L., Y.J., M.Y., and W.Z. evaluated and discussed the data. B.S. and Y.H. co-wrote the manuscript with help from M.Y. and W.Z. All authors reviewed and discussed the manuscript. **Competing interests:** W.Z. and Y.H. are inventors on a patent application submitted by the University of Colorado Boulder that covers the synthesis and composition of ICOFs having precisely tunable pores. M.Y. and B.S. are inventors on a patent application submitted by the University at Buffalo that covers the potential applications of precisely tuned pores in ICOFs. The remaining authors declare no competing interests. **Data and materials availability:** All data are available in the main text or the supplementary materials.

SUPPLEMENTARY MATERIALS

science.org/doi/10.1126/science.adj8791
Materials and Methods
Supplementary Text
Figs. S1 to S52
Tables S1 to S18
References (*45*–*91*)
Movie S1
Data S1 to S6

Submitted 20 July 2023; accepted 13 May 2024
10.1126/science.adj8791